

DOI: 10.1002/((please add manuscript number))

Article type: Communication

Ambipolar and Robust WSe₂ Field-Effect Transistors Utilizing Self-Assembled Edge Oxides

Hao Xu*, Xiaoyu Han, Wei Liu, Ping Liu, Hehai Fang, Xiao Li, Zhuangnan Li, Jian Guo, Bin Xiang, Weida Hu, Ivan P. Parkin, Jiang Wu*, Zhengxiao Guo, Huiyun Liu

Dr. H. Xu, Dr. W. Liu, X. Li, Prof. J. Wu, Prof. H. Liu

Department of Electronic and Electrical Engineering, University College London, Torrington Place, London WC1E 7JE, United Kingdom

Email: hao.xu.15@ucl.ac.uk; jiangwu@uestc.edu.cn

Dr. X. Han, Z. Li, J. Guo, Prof. I. P. Parkin, Prof. Z. Guo

Department of Chemistry, University College London, 20 Gordon St, London WC1H 0AJ, United Kingdom

Dr. W. Liu

London Centre for Nanotechnology, University College London, London WC1H 0AH, United Kingdom

P. Liu, Prof. B. Xiang

Division of Nanomaterials & Chemistry, Hefei National Research Centre for Physical Sciences at the Microscale, CAS Key Lab of Materials for Energy Conversion, University of Science and Technology of China, Hefei, Anhui 230026, China

Dr. H. Fang, Prof. W. Hu

State Key Laboratory of Infrared Physics, Shanghai Institute of Technical Physics, Chinese Academy of Sciences, 500 Yu Tian Road, Shanghai 200083, China

Dr. H. Fang

University of Chinese Academy of Sciences, 19 Yuquan Road, Beijing 100049, China

Prof. J. Wu

Institute of Fundamental and Frontier Sciences, University of Electronic Science and Technology of China, Chengdu 610054, P. R. China

Prof. Z. Guo

Department of Chemistry, The University of Hong Kong, Hong Kong, China

Prof. Z. Guo

Zhejiang Institute of Research and Innovation, The University of Hong Kong, Qingshan Lake SciTech City, Hangzhou, China.

Keywords: WSe₂, WO_x, self-passivation, field-effect transistors, density functional theory

Abstract

Transition metal oxides (TMOs) with high work function (WF) show promising properties as unipolar p-type contacts for transition metal dichalcogenides. Here, ambipolar field-effect transistors (FETs) enabled by bilayer WSe₂ with self-assembled TMOs (WO_{2.57}) as contacts are reported. Systematic material characterizations demonstrated the formation of WO_{2.57}/WSe₂ heterojunctions around nanoflake edges with Se atoms substituted by O atoms after air-

exposure, while pristine properties of WSe₂ almost sustained in inner domains. As-fabricated FETs exhibited both polarities, implying WO_{2.57} with lowered WF at edges can serve as both the p-type and n-type contact for inner WSe₂. Noteworthy, greatly reduced contact resistance and enhanced channel current were achieved, compared to the devices without WO_{2.57} contacts. Linear drain-source current relationship from 77 K to 300 K indicated the ohmic contact between edge WO_{2.57} and inner WSe₂. Density functional theory calculations further revealed the WO_{2.57}/WSe₂ heterojunction formed a barrier-less charge distribution. These nm-scale FETs possessed remarkable electrical conductivity up to ~ 2600 S/m, ultra-low leakage current down to ~ 10⁻¹² A, robustness for high voltage operation and air stability, which even outperformed pristine WSe₂ FETs. Theoretical calculations revealed the high conductivity was exclusively attributed to the air-induced WO_{2.57} and its further carrier injection to WSe₂.

1. Introduction

Inspired by the rapid development of the Internet of Things, wearable devices enabled by flexible electronics (FE) have attracted ever increasing attentions.^[1-3] Owing to remarkable nature of flexibility, conductivity, transparency and mechanical strength, atomically thin two dimensional (2D) materials are entrusted to advance integrated FE.^[4-6] Layered semiconducting transition metal dichalcogenides (TMDs) inherently possess thickness-dependent bandgaps and broadband absorption, beyond capability of conventional thin films, and thus are competitive candidates for flexible systems. Great efforts have been devoted to tailoring TMDs in order to broaden adaptability to achieve practical devices.^[7-9] Selenium based TMDs also possess the good properties as in the sulfur based ones, and open opportunities for applications in nanoelectronic and optoelectronic fields.^[10,11] However, they are sensitive to ambient conditions and air-induced oxidation is inevitable, especially at high temperature. Tungsten diselenide (WSe₂) is a representative member of the selenium based TMD family, which has a direct bandgap of 1.6 eV for monolayer (ML) and indirect bandgap of 1.2 eV for bulk.^[12] WSe₂ has not only been widely used for field-effect transistors (FETs) and photodetectors, but also

offers opportunities for studying oxidation, reduction and durability of TMDs exposed to ambient conditions.^[13,14]

When choosing proper contact materials for TMD devices aiming at performance improvement, work function (WF) is one of the most crucial factors need to be considered, which determines the contact barrier height and carrier injection routes.^[15] It has been demonstrated that TMD devices exhibited apparently varied properties and polarities with different metal contact designs. For instance, ambipolar WSe₂ FETs were obtained when using the low WF contacts, such as Ti, Ag and In, while unipolar p-type transport behavior was observed for WSe₂ FETs when using the high WF contacts, such as Pd and Au.^[10,16] Therefore, transition metal oxides (TMOs), such as MoO_x and WO_x ($x \leq 3$), are among the appropriate candidates for p-type contacts with TMDs, whose large WF up to ~ 6.8 eV and electron affinity make it very likely to form low barrier contacts for hole transport.^[17-19] As reported, typical p-type conduction FETs based on naturally n-doped MoS₂ was achieved, which was enabled by large WF MoO_x contacts.^[20] Self-limiting WO_x, synthesized via thermal ozone-exposure of WSe₂, was found to work as a p-type contact and dopant for underneath WSe₂.^[21] In addition, enhanced p-type FET performance was attained, based on selectively formed in-plane WSe₂/WO_x heterojunctions by air-heating.^[22]

TMOs can be obtained via natural self-assembly by air-exposure of TMDs due to dangling bonds at edges and defective sites at material surface. For example, it was reported that pristine WSe₂ underwent oxidation in air, forming WO_x around perimeter.^[23,24] However, most of previous studies employed synthetic TMOs for TMD contacts. Ozone, laser-irradiation and thermal oxidation have been used, leading to either stoichiometric or substoichiometric oxides, although some can barely reserve inherent properties in air for minutes to hours.^[25-27] Only experiencing a short duration of air-exposure, these as-grown TMOs usually have a WF very close to the theoretical value (6.0 eV ~ 6.8 eV), suitable for p-type contacts.^[19,20,28,29] Nevertheless, it is worth noting that long-term air-exposure can introduce excess oxygen

vacancies to TMOs, lowering the WF significantly,^[30-32] while air-exposure for devices is inevitable in terms of practical use. As a result, it is expected that the characteristics of TMOs can be tuned by the air-induced oxygen vacancies when working as contacts for TMDs. As for how exactly the impact is, it has still remained unclear and unexplored.

In this work, by utilizing the self-assembled edge oxides on WSe₂ that inevitably formed in ambient conditions, a series of back-gated FETs were fabricated based on air-exposed bilayer (BL) WSe₂. Systematic material characterizations and analysis validated the formation of WO_{2.57}/WSe₂ heterojunctions around edges of BL WSe₂ while almost pristine WSe₂ remained in inner domains. Differing from thermal oxidation in air, which produced WO₃, self-oxidation in air was a mild process and led to substoichiometric WO_{2.57} at edges of WSe₂ with more oxygen vacancies.^[27] With edge WO_{2.57} working as the contact for inner WSe₂, the FETs possessed ohmic contact and exhibited ambipolar behavior, high electrical conductivity (σ), ultra-low leakage current, robustness for very large bias and less sensitivity to ambient conditions. Theoretical simulations elucidated the ohmic contact was realized by the nearly barrierless charge distribution within the WO_{2.57}/WSe₂ heterojunction, consistent with the experimentally observed reduced contact resistance and enhanced channel current. Further theoretical study of carrier mobility and σ revealed that the high σ was achieved due to the WO_{2.57} contact. Our findings are essential toward fully understanding long term air stability of BL WSe₂ and demonstrate their application for ambipolar FETs using air-induced edge oxides as contacts. Notably, the devices even outperform pristine WSe₂ FETs and thus can potentially broaden initial applications, e.g., greatly enhanced σ and high-bias robustness are both particularly necessary for high energy density circuits, such as photovoltaic cell systems.

2. Results and Discussion

Fresh WSe₂ (F-WSe₂) nanoflakes were directly grown on SiO₂/Si substrates by a chemical vapor deposition (CVD) method under atmospheric pressure, which was detailed in our previous work and Experimental Section.^[23] The air-exposure induced oxidized WSe₂ (O-

WSe₂) nanoflakes were obtained by exposing as-grown F-WSe₂ samples to ambient conditions at temperature of ~ 22 °C and humidity of 45% for 6 months. Systematic characterizations and analysis were performed to study air-induced self-passivation effects by comparing F-WSe₂ and O-WSe₂. An atomic force microscope (AFM) image in Figure 1a shows surface topography of a triangular O-WSe₂ nanoflake covered by thicker (brighter) edges. As shown in the inset height profile, air-exposure caused a thicker perimeter with ~ 1 nm protrusion over the ~ 1.8 nm nanoflake. Previous studies demonstrated that atomically thin WSe₂ after ozone-exposure or laser-irradiated oxidation possessed thickened edges with tungsten oxides overlaid, so it was reasonable to estimate that the thickened edges of O-WSe₂ resulted from air-induced tungsten oxides.^[25,33] A few spots with increased height were distributed at the inner domains defined as the surface areas excluding edges. They can be air-induced adsorbates (such as H₂O, O₂ or hydrocarbon) or air-induced oxides as well, presumably formed at defective surface sites with dangling bonds.^[24] Nonetheless, the majority of the inner areas of this nanoflake was clean and exhibited uniform color, implying similar thickness of ~ 1.8 nm. Although this value suggested BL nature for F-WSe₂, we cannot yet judge the layer number of the triangular nanoflake before verifying that the top layer of inner and clean domains was not oxidized or substituted by oxides, as discussed by the Raman spectroscopy below.^[19,34] Figure 1b is a scanning electron microscope (SEM) image of another larger O-WSe₂ nanoflake on the same substrate, showing similar surface morphology to the triangular one in Figure 1a. For instance, most of the inner areas were smooth and exhibited uniform contrast while the edges presented noticeably dimmer contrast than the inner.

Raman spectroscopy, sensitive to crystal structures, carrier doping and vacancy defects, was employed to further identify air-exposure effects on O-WSe₂.^[35-38] In order to avoid phonon vibration from edge oxides or surface spots, the Raman scattering measurements for O-WSe₂ nanoflakes were carefully performed at the inner and clean sites. Excitation power was controlled around 0.1 mW to avoid possible local thermal oxidation. Figure 1c shows the first-

order Raman spectrum of the O-WSe₂ nanoflakes and Lorentzian fitting results, compared with the F-WSe₂. The eigen-peak frequencies of E_{2g}^1 (in-plane) and A_{1g} (out-of-plane) almost remained the same after air-exposure, even though slight broadening of full width at half maximum (FWHM) for E_{2g}^1 (from 4.0 cm⁻¹ to 4.7 cm⁻¹) and A_{1g} (from 5.9 cm⁻¹ to 8.2 cm⁻¹) was observed, which could stem from few air-induced crystal defects.^[39] Notably, Raman peak shift is usually inevitable for TMD materials when carrier doping or strain is introduced, so the unchanged eigen-peak positions revealed that the possibility of carrier concentration variation or lattice strain induced by air-exposure can be ruled out.^[19,40-42] The wavenumber difference between the two eigen-peaks is ~ 8 cm⁻¹ for both F-WSe₂ and O-WSe₂, suggesting BL configuration for F-WSe₂.^[33] The wavenumber difference of WSe₂ shows evident dependence on thickness and no peak of tungsten oxide (or selenium oxides) was observed (see the magenta Raman spectrum in Figure 1d), so it was inferred that the inner O-WSe₂ should not be oxidized and thus kept the same BL nature as F-WSe₂. Accordingly, the aforementioned AFM height of ~ 1.8 nm corresponded to the thickness of BL nature as well. Moreover, former studies revealed that the peak intensity ratio between E_{2g}^1 and A_{1g} modes was reduced (enlarged) when WSe₂ was thickened (thinned), while this value in our case was reduced after air-exposure.^[19,25,34] Obviously, reducing layer number corresponded to enlarged ratio, so showed an opposite tendency, and yet increasing layer number via exposing to air was unrealistic. Alternatively, we assumed the unchanged layer number of the inner O-WSe₂ can be reasonable and the reduced ratio should be attributed to surface oxygen/nitrogen absorption from air.^[39] To sum up, according to the peak position, FWHM and peak intensity ratio of Raman spectra, it can be concluded that the crystalline nature of inner areas of O-WSe₂ nanoflakes remained almost unaffected and thus can still retain original carrier type and concentration after long term air-exposure. This deduction on the basis of Raman spectroscopy is well supported by the prior

study using scanning tunneling microscopy, in which it demonstrated that the topmost Se layer, bandgap and Fermi level of inner BL WSe₂ were nearly unaffected after 9 week air-exposure.^[24] When incident photon energy approximately approaches to the electronic absorption band of materials, the condition for resonance Raman scattering (RRS) is obtained, and thus results in strong electron-phonon coupling in combination with first-order Raman scattering, leading to enhanced phonon oscillation and generating additional Raman-active modes.^[43,44] RRS spectrum of the O-WSe₂ nanoflake was obtained at nanoflake edges when using an excitation source of 633-nm laser.^[45] Since the penetration depth of 633-nm laser in WSe₂ was much larger than the height of edges, RRS spectrum was able to identify phonon modes from both WSe₂ and oxides.^[46] In Figure 1d (the orange curve), the two intense but almost degenerate peaks located at 249.4 cm⁻¹ and 259.5 cm⁻¹ (labelled by the two dash lines) were indexed to be the WSe₂ signatures of E_{2g}^1 and A_{1g} modes, respectively, implying the preservation of WSe₂ at edges. According to the reported Raman-active modes, red arrow labelled peaks (located at 223.5 cm⁻¹, 237.6 cm⁻¹, 373.7 cm⁻¹ and 394.4 cm⁻¹) were attributed to crystalline WSe₂ related Raman-active modes.^[27,45,47] Blue arrow labelled peaks located at 128.8 cm⁻¹ and 135.4 cm⁻¹ were assigned to fully oxidised WO₃, while the peaks at 156.1 cm⁻¹ and 301.9 cm⁻¹ were assigned to substoichiometric WO_{3-x}, indicating the presence of oxygen vacancies in edge tungsten oxides.^[48-51] It has been widely studied that air-exposure caused significant influence on oxygen deficiency in TMOs.^[28,32,52] For example, only one-hour air-exposure led to sharply reduced WF of MoO_x accompanied with obviously increased oxygen vacancies, nonetheless our six-month air-exposure.^[52] It can be thereby concluded that our WO_x possessed much larger density of oxygen vacancies and smaller work function than as-grown WO_x, such as nucleated via ozone, laser-irradiation and thermal oxidation.^[21,26,27] Notably, such great oxygen deficiency can increase hole injection barrier and lower electron affinity of WO_x effectively.^[19,53] Consequently, although WO_x was well known to act as hole dopants, hole-doping can become rather difficult in our case, which was well validated by the 633 nm RRS

spectrum. The wavenumber of E_{2g}^1 mode, sensitive to carrier concentration variation,^[42] remained almost identical to inner O-WSe₂ and F-WSe₂ (see 532 nm and 785 nm Raman spectra), indicating negligible doping process in WO_x/WSe₂ heterojunctions. However, the wavenumber difference between the two eigen-peaks increased to 10.1 cm⁻¹, larger than the signature of BL but very close to ML. This variation implied that the top layer of WSe₂ at edges was very likely oxidized, which was also verified by the XPS spectra below. Furthermore, no selenium oxide relevant peak was evidently resolved, so we assumed that air-induced edge oxidation very likely took place at selenium vacancy sites or replaced Se atoms with O atoms,^[54] as also discussed by XPS below. To summarize, this 633 nm RRS spectrum suggested formation of WO_x/WSe₂ heterojunctions with $x \leq 3$ at edges and oxygen deficiency. To further examine phonon vibrational properties of inner and clean areas of O-WSe₂ nanoflakes, a near-infrared excitation source of 785-nm laser was applied and thus the RRS spectrum was obtained for inner O-WSe₂. As shown in Figure 1d (the magenta curve), the two predominant eigen-peaks with ~ 8 cm⁻¹ wavenumber difference were clearly identified, while peak intensity of A_{1g} mode was noticeably enhanced compared to off-resonance. In contrast to the 633 nm spectrum, all the WSe₂ peaks were again resolved and yet the WO_x peaks were absent even under the resonant condition, which strongly implied pure WSe₂ was retained in the inner and clean areas of nanoflakes.

To identify specific chemical bonds and elemental proportion of WO_x/WSe₂ heterojunctions, edges of O-WSe₂ were probed by XPS. Figure 1e illustrates the XPS spectrum of the W 4f core level, analyzed by Gaussian fitting. The doublet peaks at 32.8 eV and 34.7 eV (black curves) were indexed to be W⁴⁺ 4f_{7/2} and W⁴⁺ 4f_{5/2} of W-Se bonds in O-WSe₂, respectively, whose binding energy (BE) and spin-orbit separation (ΔE) retained almost the same as F-WSe₂ reported by us previously.^[23] Compared to F-WSe₂, this unchanged feature was also observed for Se 3d_{5/2} and Se 3d_{3/2} of O-WSe₂ in Figure 1f, centered at 54.9 eV and 55.8 eV,

respectively.^[23] Both W^{4+} 4f and Se 3d core levels of O-WSe₂ inheriting the initial BEs of F-WSe₂ can further exclude the possibility of doping process in WO_x/WSe₂ heterojunctions. In Figure 1e, the doublet peaks at 35.8 eV and 38.0 eV (magenta curves) corresponded to W^{6+} 4f_{7/2} and W^{6+} 4f_{5/2} of stoichiometric WO₃, while the doublet peaks at 35.3 eV and 37.4 eV (purple curves) were assigned to W^{5+} 4f_{7/2} and W^{5+} 4f_{5/2} of substoichiometric WO_x, implying the oxygen deficiency.^[23,32,55] Thus, the observation of W-O bonds revealed the formation of air-induced WO_x with $x \leq 3$ at edges as well, consistent with the 633 nm RRS study. Quantitatively, the atomic proportion of W 4f and Se 3d was calculated to be 6.87% and 2.58%, respectively, whose ratio was ~ 2.66 and larger than the value of 0.5 for pristine WSe₂. The atomic percentage for W^{4+} 4f and the sum of W^{5+} 4f and W^{6+} 4f out of W 4f was calculated to be 19.20% and 80.80%, respectively. Accordingly, both reduced Se% and W-Se bonds indicated that approximately 81% Se atoms (out of the initial amount) were substituted by O atoms at edges after air-induced oxidation, elucidating the obtained Se 3d core level spectrum showing low signal-noise-ratio (Figure 1f). Considering the substitution ratio larger than the half, it was logical to infer that not only the top layer of edges was nearly all oxidized, but also the bottom layer was partially oxidized. The oxidation in the bottom layer can be introduced by diffusion of O atoms from either the top layer or lateral sides, which could propagate from the outmost to the internal.^[25,27] In addition, the O 1s spectrum in Figure 1g displays two peaks at 530.5 eV and 532.5 eV. Upon the reported BEs, the smaller BE one was assigned to WO_x and the larger one originated from beneath SiO₂ substrate and air-induced adsorbates, such as H₂O and O₂,^[32,56] suggesting both air-induced oxidation and absorption were occurred at edges. The atomic percentage of O 1s was calculated to be 76.89%, while the O 1s with smaller BE and larger BE held 18.54% and 81.46%, respectively. As a result, the atomic proportion of W 4f and O 1s related to oxides can be deduced to be 5.55% and 14.26%. Consequently, the x value in WO_x can be determined to be ~ 2.57, which was very close to the reported substoichiometric WO_{2.6} and further implied high density of oxygen vacancies.^[57,58]

After determining the components of edge and inner domains, conductive-AFM (c-AFM) equipped with a platinum coated tip was used to investigate electrical properties of O-WSe₂, as displayed in Figure 1h. Similar to the surface topography in the AFM and SEM images (Figure 1a and b), the c-AFM map illustrates that inner domains are surrounded by perimeter with different (brighter) color, indicating better σ for edges under the same bias voltage. This was resulted from substoichiometric WO_{2.57} at edges, which was reported to have much higher σ than pristine WSe₂ and validated by our DFT calculations below.^[26,27,29] Upon above series of material characterizations, it can be concluded that inner areas of O-WSe₂ inherited original properties of BL F-WSe₂, while thickened edges were oxidized to WO_{2.57}, forming the heterojunctions of WO_{2.57}/WSe₂ at edges. Such behavior observed after 6 month air-exposure can be attributed to the high crystallinity of our CVD grown F-WSe₂.^[23] Its high quality structure for the inner areas can be mostly free from dangling bonds, rarely providing air-induced oxidation with nucleation sites. In contrast, edges always tend to show more chemical reactivity due to more defective sites and broken symmetry of crystal lattice.

To give an insight of electronic properties of WO_{2.57}/WSe₂ heterojunctions, a $9 \times 1 \times 2$ BL WSe₂ with O atoms replacing the terminal Se atoms was modelled to mimic the experimental observation, shown in Figure 2a (side-view). Before conducting ribbon calculation, the lattice parameters for ML and BL WSe₂ were optimized at $a = 3.318 \text{ \AA}$ and 3.331 \AA , respectively. Compared with the observation in the bulk form (3.34 \AA), the lattice parameter of the BL is much closer to the bulk and the mismatch is under 0.27%.^[59] According to the band structures of ML and BL WSe₂ (Figure 2c and d), the BL narrowed the bandgap and migrated to an indirect bandgap. Notably, the spin-orbital coupling in BL reduced magnificently (0.4 meV), which was under the thermal contribution at room temperature (25 meV) and can be ignored. To obtain the reliable oxidized BL WSe₂ ribbons, ab-initio molecular dynamics (AIMD) was performed at 300 K, 500 K and 700 K, respectively. The selection of the temperature was due to the previous observation on thermal oxidation of WSe₂ edges, which was occurred at 400 °C (the

edges were oxidized to substoichiometric WO_x , $x \leq 3$), slowed at 300 °C and became negligible at 200 °C.^[27] The two extremes (Figure 2e) in each annealing approximation were selected for further optimization. The optimized structures (Figure 2a and b) showed the tilted WO_6 units composed at the ribbon terminals, which resembled the WO_3 structure built up with the WO_6 octahedral units. It has been reported that WO_3 phase transformation was occurred by tilting the WO_6 octahedral units (triclinic \rightarrow monoclinic \rightarrow orthorhombic) with increasing temperature.^[49] Through sharing the O atoms of the WO_6 units, oxygen deficiency offered defect band near the E_f and thus was helpful to gap state assisted carrier transport, contributing to the enhanced σ (Figure 1h).^[20,55]

Back-gated FETs were fabricated based on these O-WSe₂ nanoflakes via standard electron-beam lithography (EBL) and subsequent Ti/Au metallization. Considering edge oxidation features identified above, $\text{WO}_{2.57}$ at edges with higher σ can act as an intermediate layer between Ti contact and inner O-WSe₂, which formed Ti/ $\text{WO}_{2.57}$ /WSe₂ junctions and was further validated by contact resistance below. The schematic configuration and actual electrode layout of devices are depicted in Figure 3a, in which the two starred terminals were selected as drain and source electrodes. The devices were then wire-bonded to a logic chip carrier (LCC) for the following electrical measurements in the dark, as displayed in Figure 3b. The typical transfer characteristics of an O-WSe₂ FET in Figure 3c presents ambipolar behavior with V_{on} (the critical point) at ~ -90 V, but governed by electron transport, which was also observed in pristine WSe₂ contacted with Ti, Ag or In.^[10,16,21] Ambipolarity indicated $\text{WO}_{2.57}$ served as both electron and hole injection layers for inner O-WSe₂, instead of the previously reported WO_x only as a p-type contact for WSe₂.^[21] The reasons for this discrepancy were evident and interpreted below. Firstly, it has been widely demonstrated that oxygen vacancies can narrow bandgap and lower WF of TMOs greatly.^[30-32,55,60] According to the reported degradation of oxygen deficiency dependent WF for WO_x , it was reasonable to deduce the WF of $\text{WO}_{2.57}$ at edges was around 4.2 eV \sim 4.3 eV and the electron affinity was suppressed accordingly,^[55,60] both of which can be

much lower than the reported as-grown WO_x with high WF of ~ 6.6 eV suitable for p-type contacts.^[32,61] Obviously, the primary difference between our self-assembled $\text{WO}_{2.57}$ induced by 6 month air exposure and artificially as-obtained WO_x was the dissimilar WF associated with oxygen deficiency, so different device features can be expected when contacting WSe_2 . Additionally, both experimental and theoretical works have confirmed that contacts with low work function, such as Ti (4.33 eV), Ag (4.26 eV) and In (4.11 eV), are desired for achieving n-type dominant ambipolar WSe_2 FETs.^[16,20,62] Considering $\text{WO}_{2.57}$ can form a good ohmic contact with Ti as reported,^[19] it was reasonable to observe similar features in our O- WSe_2 FETs. The schematic band structures of $\text{WO}_{2.57}$ - WSe_2 junctions were constructed in Figure 3c (the insets). The Fermi level of $\text{WO}_{2.57}$ can lie between the conduction band minimum (CBM) and valence band maximum (VBM) of adjacent BL WSe_2 but much closer to CBM, similar to the Ti contact, hence forming a low barrier contact for electron injection at $V_{\text{bg}} = 0$ ($V_{\text{on}} < 0$). Such proposed ohmic n-type contacts were further demonstrated by the output characteristics in Figure 4a – e. When $V_{\text{bg}} > V_{\text{on}}$ (the right inset), the contact barrier became even smaller as gate voltage approached to larger positive bias, resulting in increased electron current. When $V_{\text{bg}} < V_{\text{on}}$ (the left inset), in contrast, the energy band of WSe_2 was bent reversely by the large negative gate voltage, leading to the Fermi level of WSe_2 closer to VBM. This conversion caused a p-type contact between edge $\text{WO}_{2.57}$ and inner WSe_2 , leading to hole current. Therefore, low WF $\text{WO}_{2.57}$ worked as the carrier injection layer when device biased rather than carrier dopant, as verified by Raman spectroscopy and XPS above (no peak shift was observed).

Figure 3d shows the typical output characteristics with small dependence on gate modulation, which can be divided into linear zone ($V_{\text{ds}} \leq 3\text{V}$) and non-linear zone ($V_{\text{ds}} > 3\text{V}$). For the linear zone, which was further confirmed in another O- WSe_2 FET on the same substrate (Figure S1), suggested the ohmic contact was formed among Ti, edge $\text{WO}_{2.57}$ and inner WSe_2 . Using the method introduced by Kim *et al* and Liu *et al*,^[16,63] the contact resistance can be roughly extracted from the linear $I_{\text{ds}}-V_{\text{ds}}$ curves at the very large V_{bg} . The contact resistance here was

estimated to be $\sim 10^5 \Omega \cdot \mu\text{m}$, much lower than the reported Ti directly contacted BL WSe₂ ($10^7 \sim 10^9 \Omega \cdot \mu\text{m}$).^[21,23] Besides, comparing our F-WSe₂ (with Ti contact) and O-WSe₂ FETs, the channel current at $V_{\text{ds}} = 1 \text{ V}$ and $V_{\text{gs}} = 0$ considerably increased from $1.5 \text{ nA}/\mu\text{m}$ to $1.4 \mu\text{A}/\mu\text{m}$.^[23] Both significant reduction of contact resistance and increase of channel current strongly indicated the involvement of WO_{2.57} in carrier transport, and thus the working contact with WSe₂ in O-WSe₂ FETs was WO_{2.57} instead of Ti. For the non-linear zone, the σ showed exponential-like growth as V_{ds} continuously increased, while no sign of current saturation was observed. With V_{ds} further enlarged, the contact barrier width can be effectively reduced, so more carriers can tunnel through the barrier, leading to gradually increased σ . Furthermore, it is well known that FETs work in the saturation region when $V_{\text{ds}} \gg V_{\text{bg}} - V_{\text{th}}$. According to the transfer curve in Figure 3c, the V_{th} was estimated to be much smaller than -100 V . Consequently, $V_{\text{bg}} - V_{\text{th}}$ became much greater than applied V_{ds} , leading to the absence of current saturation even under 8 V bias. Meanwhile, the $I_{\text{ds}}-V_{\text{ds}}$ curves in Figure 3c show a small degree of current control when V_{bg} changed, which can result from low carrier mobility of WO_x.^[26] Noteworthy, the O-WSe₂ FETs were able to successfully stand the huge V_{ds} bias as high as 8 V and V_{gs} modulation from -100 V to 100 V , and still worked in good conditions, as demonstrated by small leakage current in the range of $10^{-12} \sim 10^{-10} \text{ A}$ (Figure 3e and f). Compared to F-WSe₂, the operation bias range of the O-WSe₂ FETs was evidently expanded. This robustness and stability in automatically thin devices can be attributed to edge WO_{2.57}, which not only passivated edges effectively but also served as a robust buffer layer between Ti and inner WSe₂.^[64,65]

Next we performed transport measurements with changing temperatures in the vacuum and applied $-80 \text{ V} \sim 80 \text{ V}$ V_{gs} corresponding to the electron transport region. The temperature-dependent output characteristics measured under varied V_{gs} were shown in Figure 4a – e. As observed, the I_{ds} increased with rising temperature at all the gate bias and the linear behavior sustained for all the gate voltages and temperatures. It is worth noting that when under the same

bias conditions at room temperature ($V_{ds} = 3$ V and $V_{bg} = 0$), the I_{ds} obtained in air (Figure 3d) was $4.7 \mu\text{A}/\mu\text{m}$ while increased to $7.8 \mu\text{A}/\mu\text{m}$ in the vacuum (Figure 4c). This current enhancement stemmed from desorption and decomposition of air-induced adsorbates after pumping down to the vacuum, since adsorbates on the surface of TMDs can suppress carrier transport.^[21] In contrast, it was found that pristine WSe₂ or artificially oxidized WSe₂ with WO_x covered were enhanced by at least 100 times after removing surface adsorbates.^[16,21] Even though the improvement in our case was slight (less than two times), the channel current of O-WSe₂ FETs wherever in air or in the vacuum was still comparable to the reported ones after at least 100 times enhancement. This feature demonstrated that long term air exposure resulted in surface passivation of O-WSe₂, including edge oxidation and inner domain surface adsorption of air adsorbates, and it well stabilized nanoflakes showing less sensitivity to ambient conditions.

According to the output characteristics, temperature-dependent σ was then extracted (Figure 4f). The largest σ as high as ~ 2600 S/m was achieved when applied 80 V gate bias at room temperature, whose origin was discussed by DFT calculations below. Firstly, from the electrostatic potentials at different surfaces (denoted in the dash lines in Figure 2b) of O-WSe₂, the Se and O played the essential roles in the σ (Figure 2f – h). Even O possessed more localized electrons, it was balanced out by the larger atomic radii Se. Hence, the WO_{2.57} and WSe₂ also formed heterojunctions with a negligible potential barrier. Based on the analysis of the band structure (Figure 2d), theoretical prediction on the charge carrier mobility and σ of BL WSe₂ was carried out (detailed in Experimental Section and Supporting Information). In order to access the carrier transportation properties, the effective masses of the electron at CBM and hole at the VBM were calculated based on Equation 1 and listed in Table S1. Even the valence band located at Γ point, the energy difference between Γ and K is only 0.078 eV. Hence, both points were considered for the final evaluation. It was found that effective masses of the hole acted as light hole at Γ point and heavy hole along $\Gamma \rightarrow \text{M}$ and $\Gamma \rightarrow \text{K}$, respectively. It resulted

in the effective mass for the band which has ellipsoidal constant energy surface, and the average effective masses were calculated according to Equation S2 – S4. Based on the deformation potential approximation (DPA), it assumes carrier scattering occurs exclusively as a result of coupling between charge carriers and acoustic phonons propagating the direction of transport.^[66] Hence, the scattering time was calculated based on Equation 2 and listed in Table S2, with further determination of the elastic modulus and the deformation potential constants (Figure S3). With further simplification of the randomized scattering velocity, the electron and hole mobility were calculated according to Equation 3 and the results were listed in Table S3. According to the carrier concentration result from our previous study,^[23] the ideal σ of BL WSe₂ was 870.4 S/m, far below the experimentally observed one. As theoretical predicted σ without consideration of factors can reduce the actual performance, such as thermal contributed scatterings, defects, *etc.*, it should be the upper limit of the F-WSe₂. Hence, the results suggest this high σ should only be contributed by the air-induced WO_{2.57}.

To figure out the dominant mode of electron transfer in WO_{2.57}/WSe₂ junctions at different temperatures when devices working in the electron conduction region, the linear Arrhenius plots of the logarithm σ was plotted versus reciprocal temperature in Figure 5a. With different back-gate voltage of -80 V ~ 80V at 77 K ~ 300K, the device σ of O-WSe₂ and reciprocal temperature (1/T) obey the law of $\sigma = \sigma_{min} \exp(-W/kT)$, where σ_{min} is the minimum metallic conductance, W is the activation energy (eV), k is the Boltzmann constant, and T is the absolute temperature (K).^[67,68] An increase of the σ is observed as temperature rises in Figure 5a. According to the slope of linear fitting for Arrhenius plots, electron transport is dominated by the thermal activation energy rather than tunneling within the range of 77 K ~ 300 K with W at ~ 31.5 meV, well agreeing with previous results.^[69] Moreover, it is noticed that activation energy is increasing monotonously with back-gate voltage (Figure 5b). This deduction further suggested doping process can be negligible in WO_{2.57}/WSe₂ heterojunctions, as doping can effectively thin the contact barrier width, leading to substantial increase of tunneling electrons.

Lastly, Figure 5c – f display the corresponding leakage current curves with varied temperature when measuring transport characteristics of O-WSe₂ FETs. It is worth noting that ultra-low I_g between 10^{-14} and 10^{-13} A was obtained at 77 K and $10^{-12} \sim 10^{-11}$ A was measured from 120 K to 300 K, which can be nearly negligible and is much desired in energy-consuming friendly devices. The air-exposure induced passivated edges by WO_{2.57} can be responsible for the ultra-low leakage current, since pristine WSe₂ device rarely showed the similar features under very large bias.

3. Conclusion

In summary, back-gated FETs based on air-induced self-passivated O-WSe₂ nanoflakes were fabricated. Systematic material characterizations, including AFM, SEM, Raman spectroscopy, XPS and c-AFM were performed to study long-term air-exposure effects on F-WSe₂. Our results demonstrated the naturally assembled substoichiometric oxides of WO_{2.57} with Se atoms replaced by O atoms at edges, while inner domains almost preserved the pristine properties of BL WSe₂. The WO_{2.57}/WSe₂ heterojunctions formed around the perimeter showed negligible doping process, which can be suppressed by the high density of oxygen vacancies in WO_{2.57}. As-fabricated O-WSe₂ FETs exhibited typical ambipolar behavior, suggesting edge WO_{2.57} with greatly lowered WF can work as both the p-type and n-type contact for inner WSe₂. This differed from the reported TMD FETs with covered TMOs grown by thermal methods, possessing unipolar p-type transport features. In addition, drain-source current showed linear behavior from 77 K to 300 K accompanied with evidently reduced contact resistance and enhanced channel current, indicating the very low barrier ohmic contact between edge WO_{2.57} and inner WSe₂. In addition, a remarkable σ up to ~ 2600 S/m was achieved, outperforming pristine WSe₂ based FETs. From theoretical analysis, this high σ was exclusively boosted by WO_{2.57} at edges. Due to self-passivated dangling bonds of edges via air-exposure, the FETs also exhibited ultra-low leakage current, robustness for ultra-high bias and less sensitivity to ambient conditions. The atomically thin WSe₂ with self-assembled tungsten oxides in air opens new

opportunities for the edge-engineering of 2D materials for various electronic or optoelectronic devices.

4. Experimental Section

Material synthesis: The atomic-layer WSe₂ was synthesized by a chemical vapor deposition (CVD) method at atmospheric pressure. The synthesis was conducted by using a conventional horizontal quartz tube furnace. Typically, Se powders (30 mg) loaded in an alumina boat were placed at the upstream of the furnace. Another alumina boat loaded with WO₃ powders (400 mg) was located at the downstream, with the distance of ~ 20 cm away from the Se precursor. Then, a pre-cleaned SiO₂/Si (300 nm) substrate was placed face down on top of the WO₃ powders. The mixture carrier gas of argon and hydrogen (5%) gas was purged through the furnace prior to the heating process. After that, the furnace was heated up to 925 °C in 30 min and maintained at this temperature for 10 min. Subsequently, furnace was cooled down to 850 °C in 40 min and kept at 850 °C for 15 min. Then, the furnace was naturally cooled to room temperature. During the whole growth process, the CVD system was protected with a constant flow rate of 50 sccm carrier gas under atmospheric pressure.

Material characterizations: The morphology of WSe₂ nanosheets and devices was obtained using scanning electron microscopy (SEM, Carl Zeiss Orion NanoFab, 20 kV), and the nanosheet thickness was confirmed by AFM (Bruker Dimension Icon, tapping mode). X-ray photoelectron spectroscopy (XPS equipped with a monochromatic Al K α X-ray source, Thermo Fisher Escalab 250Xi) was employed to characterize the elemental composition in air-exposed WSe₂. Raman spectroscopy was performed using a confocal Raman spectrometer (Horiba Jobin Yvon HR Evolution) with laser spot diameter of ~ 1 μ m. To avoid possible laser-induced thermal effect, the laser power was controlled at ~ 0.1 mW. The current-mapping measurements were carried out in a Keysight 5600LS atomic force microscopy (AFM) with the current sensing mode in air.

Device fabrication and measurement: The contact terminals of back-gated FETs were patterned using e-beam lithography (EBL) and then metallization using e-beam evaporation of Ti/Au (10 nm/50 nm). The electrical measurement was conducted at the Lake Shore four-probe semiconductor analyzing system, equipped with a Keithley 4200 semiconductor parameter analyzer.

DFT calculation: All the calculations were carried out based on spin-polarized Density Functional Theory (DFT), implanted in Vienna *ab-initio* Package (VASP) and employing the projector-augmented-wave theory.^[70,71] The kinetic energy cutoff was set to 500 eV for the plane wave basis. The PBE functions were employed for describing the electronic exchange-correlation (XC) for all bulk, ML and BL WSe₂.^[72] Due to the unneglectable Δ_{SO} of WSe₂, spin-orbital coupling was also considered in all the calculations, as well as dipole correction along the out-of-plane direction.^[73,74] For BL WSe₂, the van der Waals correction was adopted the Grimme method.^[75] The dipole corrections were considered in all the calculations. The AIMD calculations were performed at 300, 500 and 700 K with the Nose–Hoover method and lasted for 1 ps with 1 fs intervals for each ionic movement.^[76]

The effective mass of holes (m_h^*) at the valence band maximum and electrons (m_e^*) at the conduction band minimum were calculated based on

$$m^* = \hbar^2 \left(\frac{\partial^2 E}{\partial k^2} \right)^{-1} \quad (1)$$

Where E and K correspond to the energy and the reciprocal vectors along different direction along Γ -M-K.

The charge carriers scattering time (τ) were simplified to only consider the coupling between charge carrier and acoustic phonons in the transport direction. According to the deformation potential approximation (DPA), the scattering time was calculated according to the following equation:^[77]

$$\tau = \frac{\hbar^3 C_{2D}}{k_B T m^* E_d^2} \quad (2)$$

Where C_{2D} is the elastic modulus along the transport direction, \hbar and k_B is the reduced Plank the Boltzmann constant, respectively, T is the temperature, which was set at room temperature and E_d is the deformation potential constant.

Then, assuming the charge carrier velocity is random after each scattering, the charge carrier mobility (μ) was calculated in the following equation. The calculated carrier mobility was listed in Table S3.

$$\mu = \frac{q}{m^*} \tau \quad (3)$$

Finally, the conductivity was calculated based on

$$\sigma = en\mu \quad (4)$$

Where e is the electron charge, n is the carrier concentration, obtained from our previous experimental result ($1.11 \times 10^{18} \text{ cm}^{-3}$).^[23] Detailed calculation was listed in Supporting Information.

Supporting Information

Supporting Information is available from the Wiley Online Library or from the author.

Acknowledgements

This work was supported by grants from the UK EPSRC Future Compound Semiconductor Manufacturing Hub (EP/P006973/1) and EPSRC grants (EP/N032888/1 and EP/L018330/1). The authors also acknowledge the use of the UCL Grace High Performance Computing Facility (Grace@UCL) and associated support services. Dr. Hao Xu and Jian Guo would like to acknowledge the China Scholarship Council (CSC).

References

- [1] C. Choi, M. K. Choi, S. Liu, M. S. Kim, O. K. Park, C. Im, J. Kim, X. Qin, G. J. Lee, K. W. Cho, M. Kim, E. Joh, J. Lee, D. Son, S. H. Kwon, N. L. Jeon, Y. M. Song, N. Lu, D. H. Kim, *Nat. Commun.* **2017**, *8*, 1664.
- [2] J. M. Nassar, S. M. Khan, D. R. Villalva, M. M. Nour, A. S. Almuslem, M. M. Hussain, *npj Flex. Electron.* **2018**, *2*, 24.
- [3] A. Sarycheva, A. Polemi, Y. Liu, K. Dandekar, B. Anasori, Y. Gogotsi, *Sci. Adv.* **2018**, *4*, eaau0920.

- [4] D. Akinwande, N. Petrone, J. Hone, *Nat. Commun.* **2015**, *5*, 5678.
- [5] K. S. Novoselov, A. Mishchenko, A. Carvalho, A. H. Castro Neto, *Science*. **2016**, *353*, 9439.
- [6] J. Zhu, H. Xu, G. Zou, W. Zhang, R. Chai, J. Choi, J. Wu, H. Liu, G. Shen, H. Fan, *J. Am. Chem. Soc.* **2019**, *141*, 5392.
- [7] K. F. Mak, J. Shan, *Nat. Photonics* **2016**, *10*, 216.
- [8] C. Xie, C. Mak, X. Tao, F. Yan, *Adv. Funct. Mater.* **2017**, *27*, 1603886.
- [9] H. Xu, X. Han, X. Dai, W. Liu, J. Wu, J. Zhu, D. Kim, G. Zou, K. A. Sablon, A. Sergeev, Z. Guo, H. Liu, *Adv. Mater.* **2018**, *30*, 1706561.
- [10] W. Zhang, M.-H. Chiu, C.-H. Chen, W. Chen, L. Li, A. T. S. Wee, W. Monolayers, W. Zhang, M.-H. Chiu, C.-H. Chen, W. Chen, L. Li, *ACS Nano* **2014**, *8*, 8653.
- [11] B. W. H. Baugher, H. O. H. Churchill, Y. Yang, P. Jarillo-Herrero, *Nat. Nanotechnol.* **2014**, *9*, 262.
- [12] H. Fang, S. Chuang, T. C. Chang, K. Takei, T. Takahashi, A. Javey, *Nano Lett.* **2012**, *12*, 3788.
- [13] S. H. H. Shokouh, P. J. Jeon, A. Pezeshki, K. Choi, H. S. Lee, J. S. Kim, E. Y. Park, S. Im, *Adv. Funct. Mater.* **2015**, *25*, 7208.
- [14] Z. Yang, L. Liao, F. Gong, F. Wang, Z. Wang, X. Liu, X. Xiao, W. Hu, J. He, X. Duan, *Nano Energy* **2018**, *49*, 103.
- [15] A. Allain, J. Kang, K. Banerjee, A. Kis, *Nat. Mater.* **2015**, *14*, 1195.
- [16] W. Liu, J. Kang, D. Sarkar, Y. Khatami, D. Jena, K. Banerjee, *Nano Lett.* **2013**, *13*, 1983.
- [17] S. McDonnell, A. Azcatl, R. Addou, C. Gong, C. Battaglia, S. Chuang, K. Cho, A. Javey, R. M. Wallace, *ACS Nano* **2014**, *8*, 6265.
- [18] M. Gratzel, *Nature* **2001**, *414*, 338.
- [19] R. Zhang, D. Drysdale, V. Koutsos, R. Cheung, *Adv. Funct. Mater.* **2017**, *27*, 1702455.
- [20] S. Chuang, C. Battaglia, A. Azcatl, S. McDonnell, J. S. Kang, X. Yin, M. Tosun, R. Kapadia, H. Fang, R. M. Wallace, A. Javey, *Nano Lett.* **2014**, *14*, 1337.
- [21] M. Yamamoto, S. Nakaharai, K. Ueno, K. Tsukagoshi, *Nano Lett.* **2016**, *16*, 2720.
- [22] B. Liu, A. Zhang, L. Chen, A. N. Abbas, Y. Liu, C. Shen, H. Wan, C. Zhou, *ACS Nano* **2016**, *10*, 5153.
- [23] J. Huang, L. Yang, D. Liu, J. Chen, Q. Fu, Y. Xiong, F. Lin, B. Xiang, *Nanoscale* **2015**, *7*, 4193.
- [24] J. H. Park, S. Vishwanath, X. Liu, H. Zhou, S. M. Eichfeld, S. K. Fullerton-Shirey, J. A. Robinson, R. M. Feenstra, J. Furdyna, D. Jena, H. G. Xing, A. C. Kummel, *ACS Nano* **2016**, *10*, 4258.
- [25] M. Yamamoto, S. Dutta, S. Aikawa, S. Nakaharai, K. Wakabayashi, M. S. Fuhrer, K. Ueno, K. Tsukagoshi, *Nano Lett.* **2015**, *15*, 2067.
- [26] C. Tan, Y. Liu, H. Chou, J. S. Kim, D. Wu, D. Akinwande, K. Lai, *Appl. Phys. Lett.* **2016**, *108*, 083112.
- [27] Y. Liu, C. Tan, H. Chou, A. Nayak, D. Wu, R. Ghosh, H. Y. Chang, Y. Hao, X. Wang, J. S. Kim, R. Piner, R. S. Ruoff, D. Akinwande, K. Lai, *Nano Lett.* **2015**, *15*, 4979.
- [28] M. T. Greiner, L. Chai, M. G. Helander, W. M. Tang, Z. H. Lu, *Adv. Funct. Mater.* **2012**, *22*, 4557.
- [29] H. Zheng, J. Z. Ou, M. S. Strano, R. B. Kaner, A. Mitchell, K. Kalantar-Zadeh, *Adv. Funct. Mater.* **2011**, *21*, 2175.
- [30] S. Won, S. Y. Lee, J. Park, H. Seo, *Sci. Rep.* **2017**, *7*, 10186.
- [31] Irfan, H. Ding, Y. Gao, C. Small, D. Y. Kim, J. Subbiah, F. So, *Appl. Phys. Lett.* **2010**, *96*, 243307.
- [32] L. Fang, S. J. Baik, J. W. Kim, S. J. Kang, J. W. Seo, J. W. Jeon, Y. H. Kim, K. S. Lim, *J. Appl. Phys.* **2011**, *109*, 104501.

- [33] H. Li, G. Lu, Y. Wang, Z. Yin, C. Cong, Q. He, L. Wang, F. Ding, T. Yu, H. Zhang, *Small* **2013**, *9*, 1974.
- [34] P. Tonndorf, R. Schmidt, P. Böttger, X. Zhang, J. Börner, A. Liebig, M. Albrecht, C. Kloc, O. Gordan, D. R. T. Zahn, S. M. de Vasconcellos, R. Bratschitsch, *Opt. Express* **2013**, *21*, 4908.
- [35] H. Xu, Y. Song, W. Pan, Q. Chen, X. Wu, P. Lu, Q. Gong, S. Wang, *AIP Adv.* **2015**, *5*, 87103.
- [36] H. Xu, Y. Song, Q. Gong, W. Pan, X. Wu, S. Wang, *Mod. Phys. Lett. B* **2015**, *29*, 1550075.
- [37] W. Pan, J. A. Steele, P. Wang, K. Wang, Y. Song, L. Yue, X. Wu, H. Xu, Z. Zhang, S. Xu, P. Lu, L. Wu, Q. Gong, S. Wang, *Semicond. Sci. Technol.* **2015**, *30*, 094003.
- [38] H. Xu, X. Han, Z. Li, W. Liu, X. Li, J. Wu, Z. Guo, H. Liu, *Adv. Mater. Interfaces* **2018**, *5*, 1801048.
- [39] Q. Qian, Z. Zhang, K. J. Chen, *Langmuir* **2018**, *34*, 2882.
- [40] A. Khosravi, R. Addou, C. M. Smyth, R. Yue, C. R. Cormier, J. Kim, C. L. Hinkle, R. M. Wallace, *APL Mater.* **2018**, *6*, 026603.
- [41] D. H. Kang, J. Shim, S. K. Jang, J. Jeon, M. H. Jeon, G. Y. Yeom, W. S. Jung, Y. H. Jang, S. Lee, J. H. Park, *ACS Nano* **2015**, *9*, 1099.
- [42] K. Chen, D. Kiriya, M. Hettick, M. Tosun, T. J. Ha, S. R. Madhupathy, S. Desai, A. Sachid, A. Javey, *APL Mater.* **2014**, *2*, 092504.
- [43] C. Sourisseau, F. Cruege, M. Fouassier, M. Alba, *Chem. Phys.* **1991**, *150*, 281.
- [44] A. M. Stacy, D. T. Hodul, *J. Phys. Chem. Solids* **1985**, *46*, 405.
- [45] S. V. Bhatt, M. P. Deshpande, V. Sathe, R. Rao, S. H. Chaki, *J. Raman Spectrosc.* **2014**, *45*, 971.
- [46] M. Placidi, M. Dimitrievska, V. Izquierdo-Roca, X. Fontané, A. Castellanos-Gomez, A. Pérez-Tomás, N. Mestres, M. Espindola-Rodriguez, S. López-Marino, M. Neuschitzer, V. Bermudez, A. Yaremko, A. Pérez-Rodríguez, *2D Mater.* **2015**, *2*, DOI 10.1088/2053-1583/2/3/035006.
- [47] E. Del Corro, H. Terrones, A. Elias, C. Fantini, S. Feng, M. A. Nguyen, T. E. Mallouk, M. Terrones, M. A. Pimenta, *ACS Nano* **2014**, *8*, 9629.
- [48] J. Guo, Y. Li, S. Zhu, Z. Chen, Q. Liu, D. Zhang, W.-J. Moon, D.-M. Song, *RSC Adv.* **2012**, *2*, 1356.
- [49] C. V. Ramana, S. Utsunomiya, R. C. Ewing, C. M. Julien, U. Becker, *J. Phys. Chem. B* **2006**, *110*, 10430.
- [50] J. Chen, D. Lu, W. Zhang, F. Xie, J. Zhou, L. Gong, X. Liu, S. Deng, N. Xu, *J. Phys. D. Appl. Phys.* **2008**, *41*, 115305.
- [51] K. Thummavichai, N. Wang, F. Xu, G. Rance, Y. Xia, Y. Zhu, *R. Soc. Open Sci.* **2018**, *5*, 171932.
- [52] I. Irfan, A. James Turinske, Z. Bao, Y. Gao, *Appl. Phys. Lett.* **2012**, *101*, 093305.
- [53] T. Zheng, W. Sang, Z. He, Q. Wei, B. Chen, H. Li, C. Cao, R. Huang, X. Yan, B. Pan, S. Zhou, J. Zeng, *Nano Lett.* **2017**, *17*, 7968.
- [54] M. Yamamoto, T. L. Einstein, M. S. Fuhrer, W. G. Cullen, *J. Phys. Chem. C* **2013**, *117*, 25643.
- [55] Z. Zhang, H. X. Wei, G. F. Ma, Y. Q. Li, S. T. Lee, J. X. Tang, *Appl. Phys. Lett.* **2013**, *103*, 133302.
- [56] D. Y. Lu, J. Chen, J. Zhou, S. Z. Deng, N. S. Xu, J. B. Xu, *J. Raman Spectrosc.* **2007**, *38*, 176.
- [57] V. A. Arslambekov, *Prot. Met.* **2003**, *39*, 99.
- [58] P. Uppachai, V. Harnchana, S. Pimanpang, V. Amornkitbamrung, A. P. Brown, R. M. D. Brydson, *Electrochim. Acta* **2014**, *145*, 27.
- [59] W. J. Schutte, J. L. De Boer, F. Jellinek, *J. Solid State Chem.* **1987**, *70*, 207.

- [60] M. Mews, L. Korte, B. Rech, *Sol. Energy Mater. Sol. Cells* **2016**, *158*, 77.
- [61] J. Meyer, M. Kröger, S. Hamwi, F. Gnam, T. Riedl, W. Kowalsky, A. Kahn, *Appl. Phys. Lett.* **2010**, *96*, 193302.
- [62] J. Kang, W. Liu, D. Sarkar, D. Jena, K. Banerjee, *Phys. Rev. X* **2014**, *4*, 031005.
- [63] S. Kim, A. Konar, W. S. Hwang, J. H. Lee, J. Lee, J. Yang, C. Jung, H. Kim, J. B. Yoo, J. Y. Choi, Y. W. Jin, S. Y. Lee, D. Jena, W. Choi, K. Kim, *Nat. Commun.* **2012**, *3*, 1011.
- [64] M. H. Hekmatshoar, M. Mirzayi, M. Mirzayi, *Ionics (Kiel)*. **2010**, *16*, 185.
- [65] A. Ablat, A. Kyndiah, G. Houin, T. Y. Alic, L. Hirsch, M. Abbas, *Sci. Rep.* **2019**, *9*, 6685.
- [66] J. Bardeen, W. Shockley, *Phys. Rev.* **1950**, *80*, 72.
- [67] M. Pepper, *Philos. Mag. B* **1978**, *37*, 83.
- [68] M. Pepper, *J. Non. Cryst. Solids* **1979**, *32*, 161.
- [69] X. X. Zhang, Y. You, S. Y. F. Zhao, T. F. Heinz, *Phys. Rev. Lett.* **2015**, *115*, 257403.
- [70] G. Kresse, D. Joubert, *Phys. Rev. B* **1999**, *59*, 1758.
- [71] G. Kresse, J. Furthmüller, *Phys. Rev. B - Condens. Matter Mater. Phys.* **1996**, *54*, 11169.
- [72] J. P. Perdew, K. Burke, M. Ernzerhof, *Phys. Rev. Lett.* **1996**, *77*, 3865.
- [73] Y. Zhang, M. M. Ugeda, C. Jin, S.-F. Shi, A. J. Bradley, A. Martín-Recio, H. Ryu, J. Kim, S. Tang, Y. Kim, B. Zhou, C. Hwang, Y. Chen, F. Wang, M. F. Crommie, Z. Hussain, Z.-X. Shen, S.-K. Mo, *Nano Lett.* **2016**, *16*, 2485.
- [74] C. Zhang, Y. Chen, A. Johnson, M.-Y. Li, L.-J. Li, P. C. Mende, R. M. Feenstra, C.-K. Shih, *Nano Lett.* **2015**, *15*, 6494.
- [75] S. Grimme, *J. Comput. Chem.* **n.d.**, *27*, 1787.
- [76] H. C. Andersen, *J. Chem. Phys.* **1980**, *72*, 2384.
- [77] J. Xi, M. Long, L. Tang, D. Wang, Z. Shuai, *Nanoscale* **2012**, *4*, 4348.

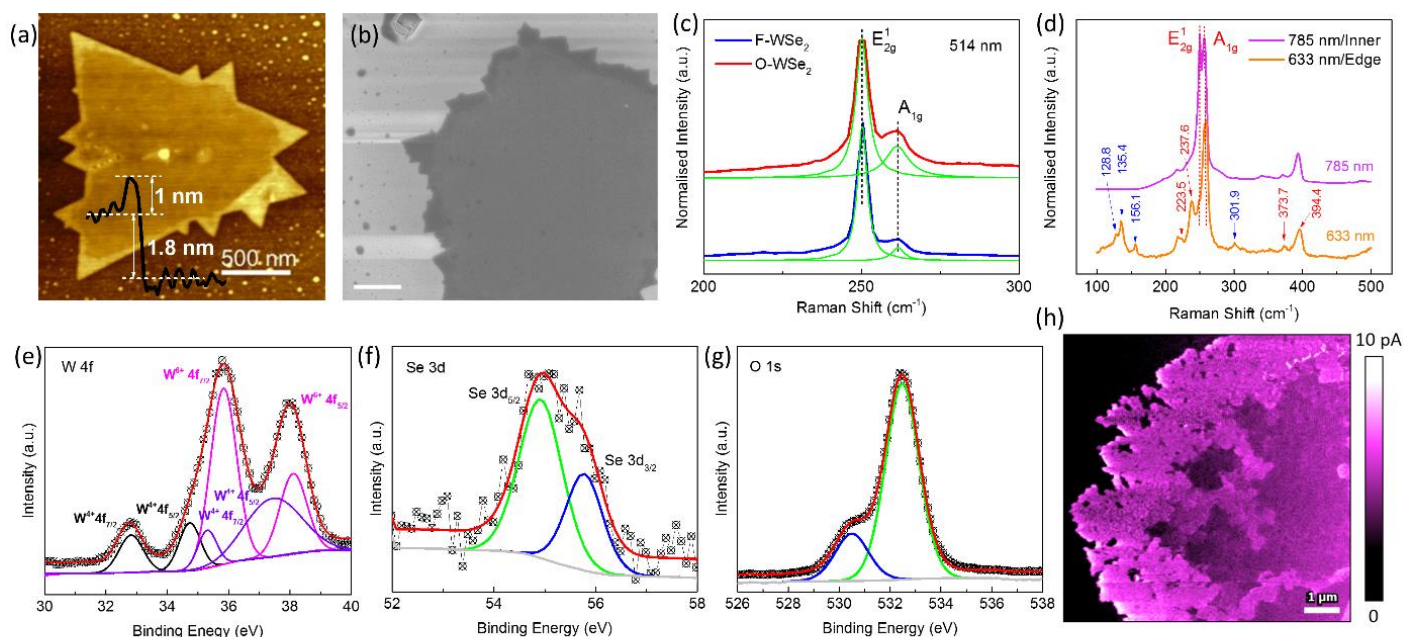


Figure 1. Material characterization results of air-exposed BL O-WSe₂ nanoflakes on the same SiO₂/Si substrate. (a) An AFM image of a triangular O-WSe₂ domain with a height profile inserted. The scale bar is 500 nm. (b) An SEM image of an O-WSe₂ domain with larger scale. The scale bar is 1 μm. (c) Off-resonance Raman spectra of F-WSe₂ (blue curve) and O-WSe₂ (red curve) nanoflakes, excited by a 514-nm laser source. The green curves are fitted peaks. (d) RRS spectra using 633-nm (orange curve) and 785-nm (magenta curve) excitation sources, which were obtained at the edge and the inner area of O-WSe₂, respectively. (e – g) Binding energy profiles of W 4f, Se 3d and O 1s, respectively, obtained at the edge. The scattered dots and red curves represent measured data and fitting curves, respectively. (h) The c-AFM map of an O-WSe₂ domain. The scale bar is 1 μm.

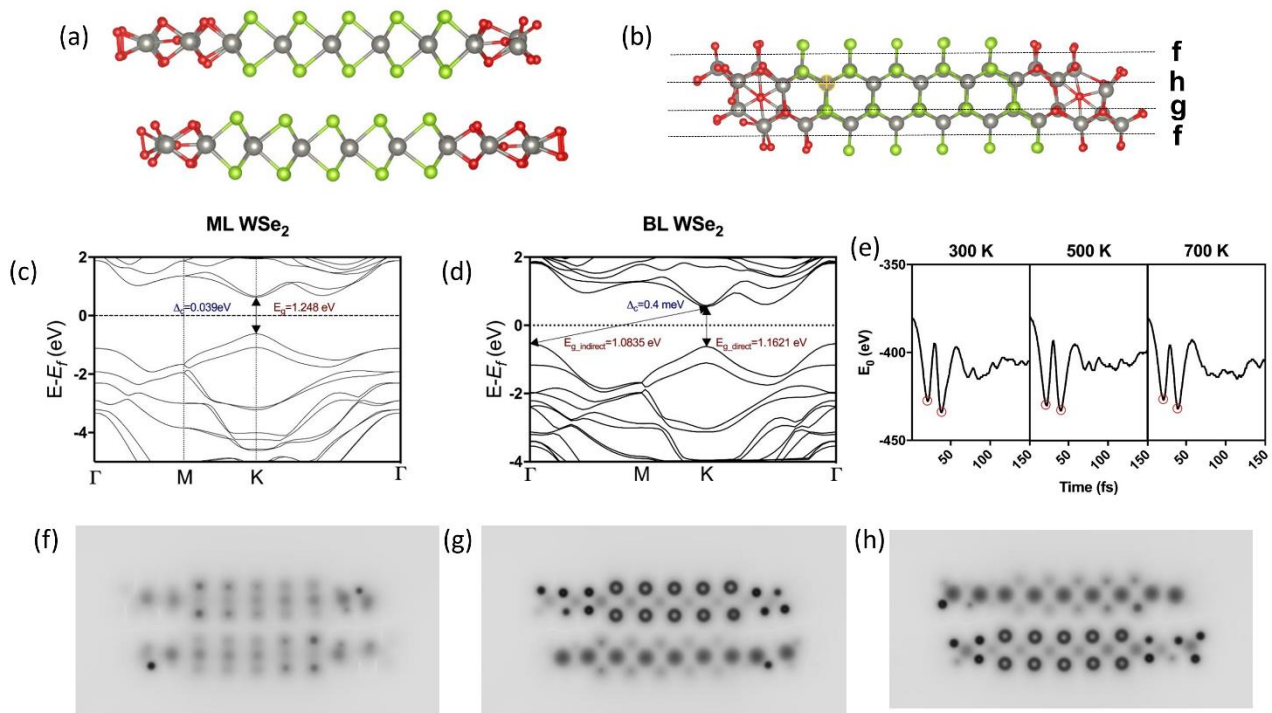


Figure 2. DFT calculation models and results. (a) The side-view of the optimized structure for the $9 \times 1 \times 2$ BL WSe₂ with O atoms replacing the terminal Se atoms. (b) The top-view of the oxidized BL WSe₂ ribbon. The dash lines represent the surfaces carried out the static electron potential calculations, resulted in figure (f), (g) and (h). The band structure of (c) ML WSe₂ and (d) BL WSe₂. From ML to BL, the direct bandgap migrates to indirect. And the spin-orbital coupling effect reduced magnificently. (e) The ab-initio MD calculation at 300 K, 500 K and 700 K for the optimized oxidized WSe₂ nanoribbon. The red circle highlighted the top two extremes at each AIMD, and these configurations were further conducted with structural optimizations. The final optimized structure was shown in (a) and (b).

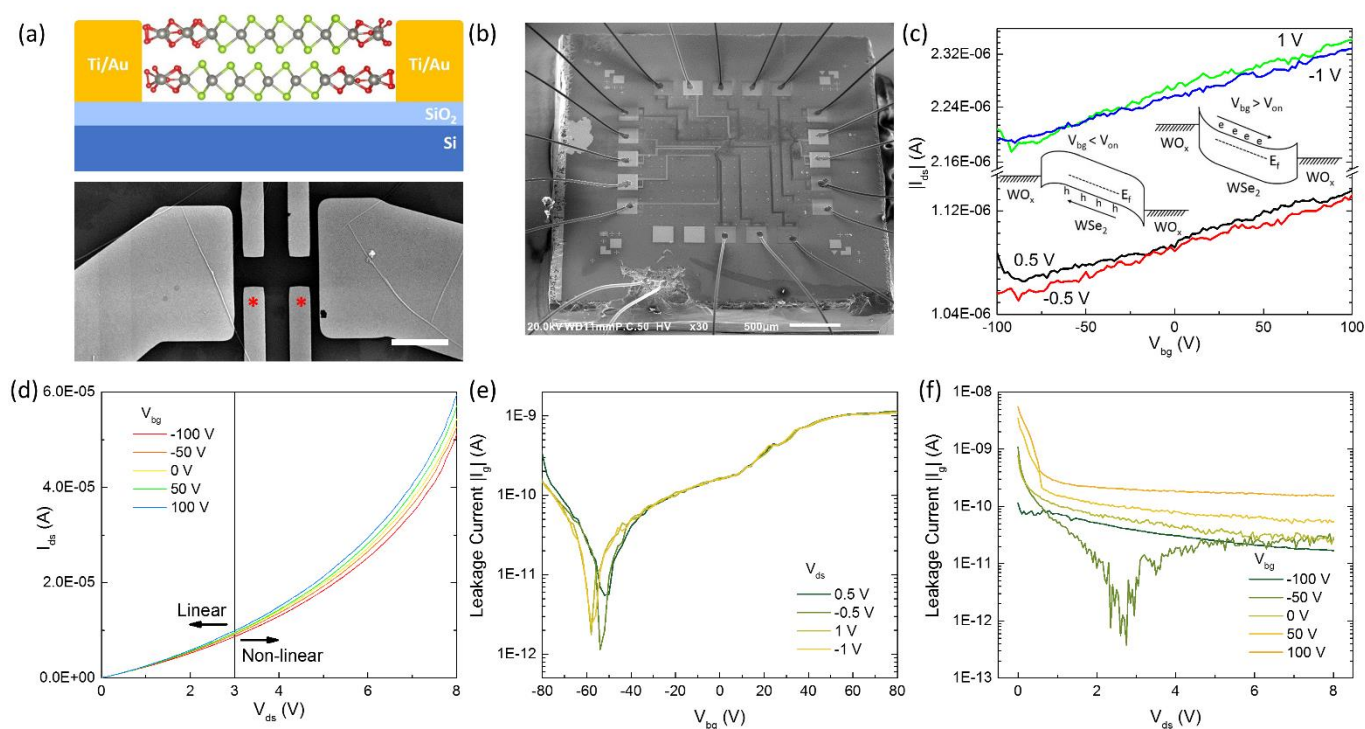


Figure 3. Configurations and carrier transport characteristics of O-WSe₂ FETs in the dark. (a) The schematic image (upper) of an FET based on a BL O-WSe₂ nanoflake and the SEM image (lower) of the realistic electrode layout, the scale bar is 5 μm . (b) An SEM image of devices wire-bonded to the LCC. (c) Transfer characteristics of the O-WSe₂ FET at room temperature. The insets describe the schematic band structures of WO_{2.57}/WSe₂ junctions when the device is biased. (d) Output characteristics of the FET at room temperature, divided into linear and non-linear regions. (e, f) Leakage current plots versus back-gate and drain-source bias, respectively, showing very tiny gate leak.

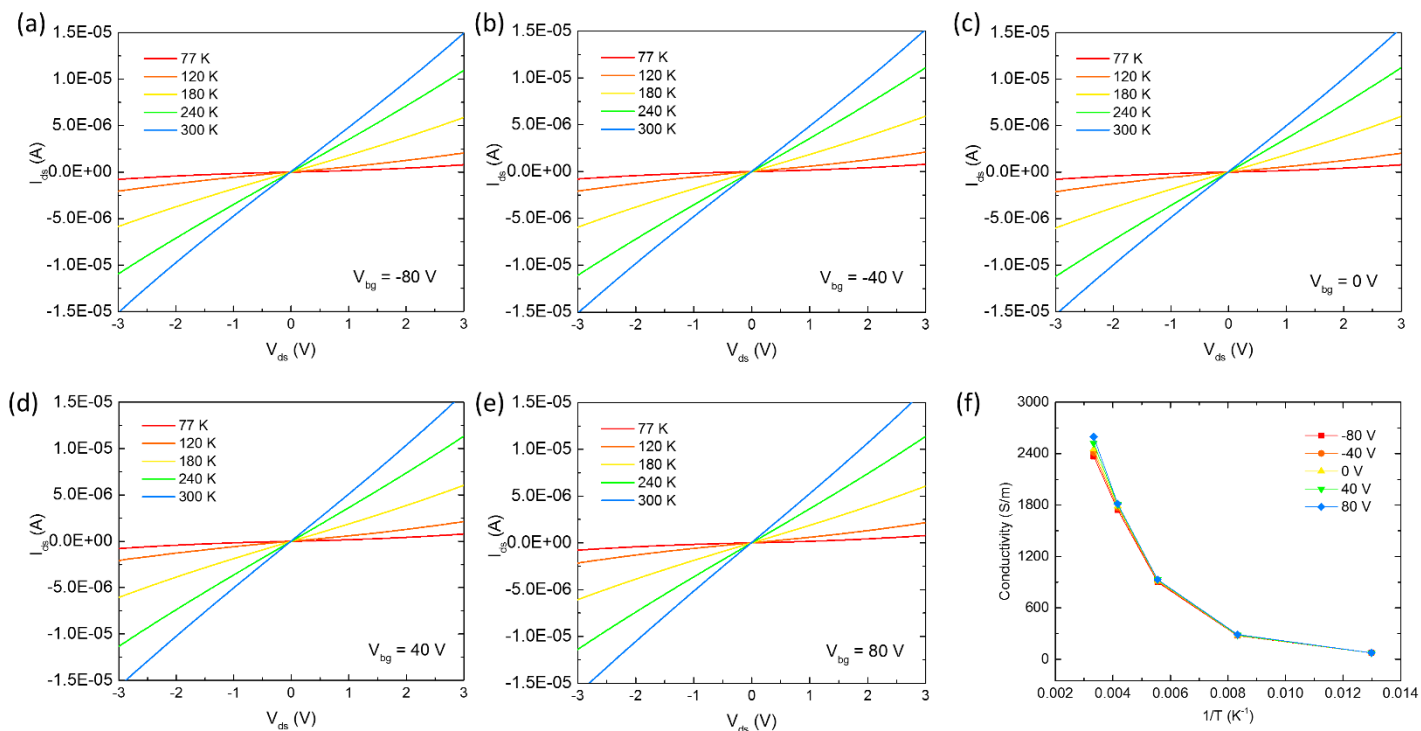


Figure 4. Electrical transport features with changing temperature of the FETs when working at the electron transport dominant region ($V_{bg} > V_{on}$). (a – e) Temperature-dependent (from 77 K to 300 K) output characteristics under different back-gate voltages (from -80 V to 80 V), respectively. (f) Electrical conductivity extracted from changing temperatures (from 77 K to 300 K) and back-gate voltages (from -80 V to 80 V).

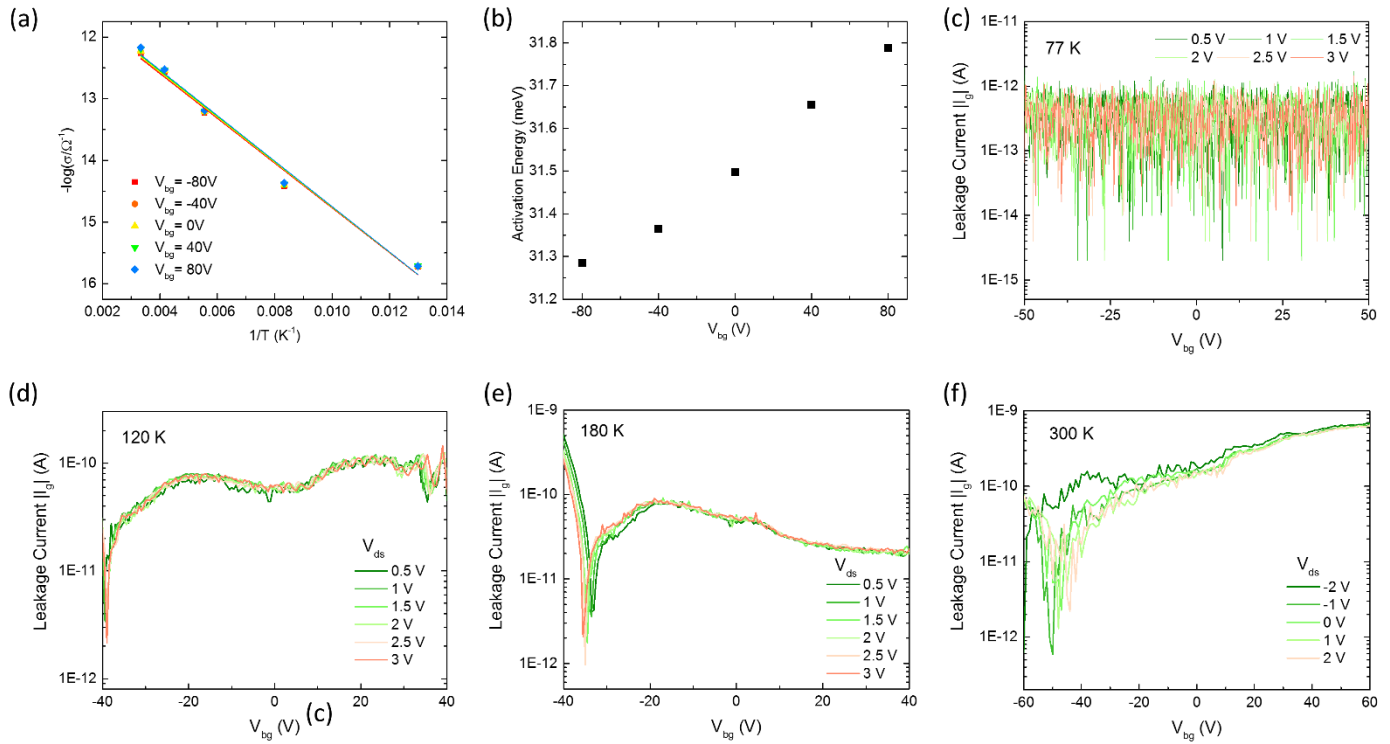


Figure 5. Temperature-dependent activation energy analysis and the ultra-low leakage current of the O-WSe₂ FETs. (a) Logarithm of electrical conductivity as a function of reciprocal temperature ($1/T$) for the O-WSe₂ FETs in various back-gate voltage of -80 V ~ 80 V at 77 K ~ 300 K. (b) The V_{bg} dependent activation energy of electrons in O-WSe₂ is estimated from linear Arrhenius plots in (a). (c – f) Leakage current curves of the O-WSe₂ FETs when measuring the transport characteristics under varied temperatures (from 77 K ~ 300 K).

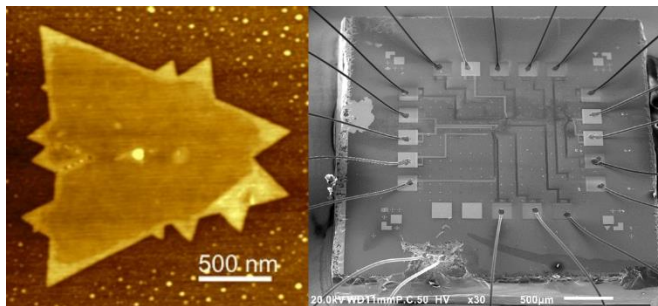
The table of contents entry

Field-effect transistors based on air-induced self-passivated bilayer WSe₂ are reported. Systematic material characterizations validated the formation of WO_{2.57}/WSe₂ heterojunctions around edges of WSe₂ while pristine WSe₂ remained in inner domains. With WO_{2.57} working as the contact for WSe₂, FETs possessed ohmic contact and ambipolar behavior, high conductivity, ultra-low leakage current, robustness for ultra-high voltage and less sensitivity to ambient conditions.

Keywords: WSe₂, WO_x, self-passivation, field-effect transistors, density functional theory

Hao Xu*, Xiaoyu Han, Wei Liu, Ping Liu, Hehai Fang, Xiao Li, Zhuangnan Li, Jian Guo, Bin Xiang, Weida Hu, Ivan P. Parkin, Jiang Wu*, Zhengxiao Guo, Huiyun Liu

Title Ambipolar and Robust WSe₂ Field-Effect Transistors Utilizing Self-Assembled Edge Oxides



Supporting Information

Title Ambipolar and Robust WSe₂ Field-Effect Transistors Utilizing Self-Assembled Edge Oxides

Hao Xu*, Xiaoyu Han, Wei Liu, Ping Liu, Hehai Fang, Xiao Li, Zhuangnan Li, Jian Guo, Bin Xiang, Weida Hu, Ivan P. Parkin, Jiang Wu*, Zhengxiao Guo, Huiyun Liu

Dr. H. Xu, Dr. W. Liu, X. Li, Prof. J. Wu, Prof. H. Liu
Department of Electronic and Electrical Engineering, University College London, Torrington Place, London WC1E 7JE, United Kingdom

Email: hao.xu.15@ucl.ac.uk; jiangwu@uestc.edu.cn

Dr. X. Han, Z. Li, J. Guo, Prof. I. P. Parkin, Prof. Z. Guo
Department of Chemistry, University College London, 20 Gordon St, London WC1H 0AJ, United Kingdom

Dr. W. Liu
London Centre for Nanotechnology, University College London, London WC1H 0AH, United Kingdom

P. Liu, Prof. B. Xiang
Division of Nanomaterials & Chemistry, Hefei National Research Centre for Physical Sciences at the Microscale, CAS Key Lab of Materials for Energy Conversion, University of Science and Technology of China, Hefei, Anhui 230026, China

Dr. H. Fang, Prof. W. Hu
State Key Laboratory of Infrared Physics, Shanghai Institute of Technical Physics, Chinese Academy of Sciences, 500 Yu Tian Road, Shanghai 200083, China

Dr. H. Fang
University of Chinese Academy of Sciences, 19 Yuquan Road, Beijing 100049, China

Prof. J. Wu
Institute of Fundamental and Frontier Sciences, University of Electronic Science and Technology of China, Chengdu 610054, P. R. China

Prof. Z. Guo
Department of Chemistry, The University of Hong Kong, Hong Kong, China

Prof. Z. Guo
Zhejiang Institute of Research and Innovation, The University of Hong Kong, Qingshan Lake SciTech City, Hangzhou, China.

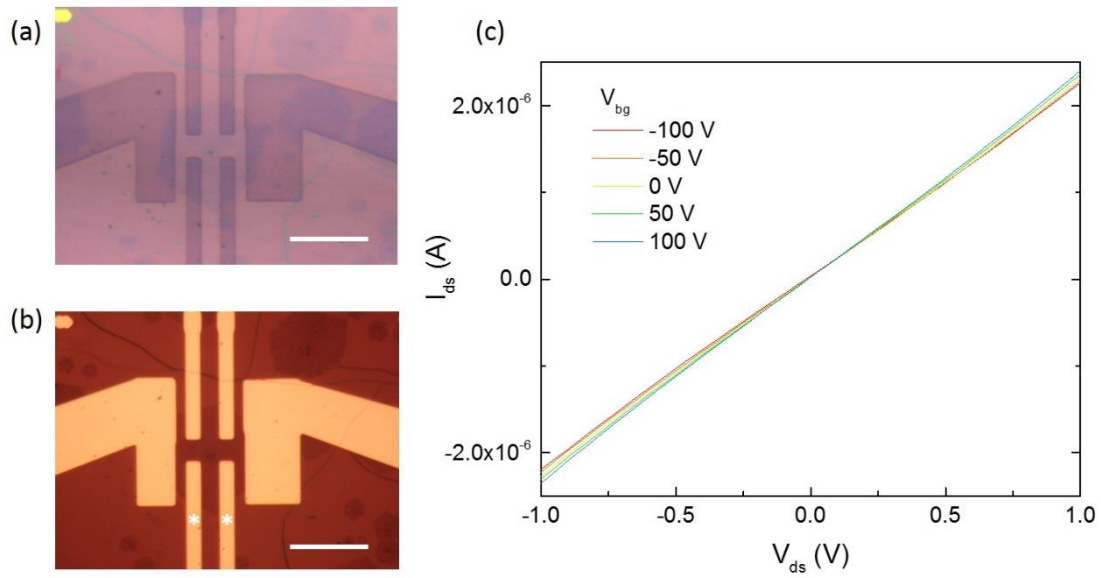


Figure S1. Optical microscope images (a) after EBL patterning and (b) after metallization, obtained in the process of fabricating a BL O-WSe₂ based FET. The scale bar is 10 μm . (c) Room temperature output curves of the BL O-WSe₂ FET, showing ohmic features.

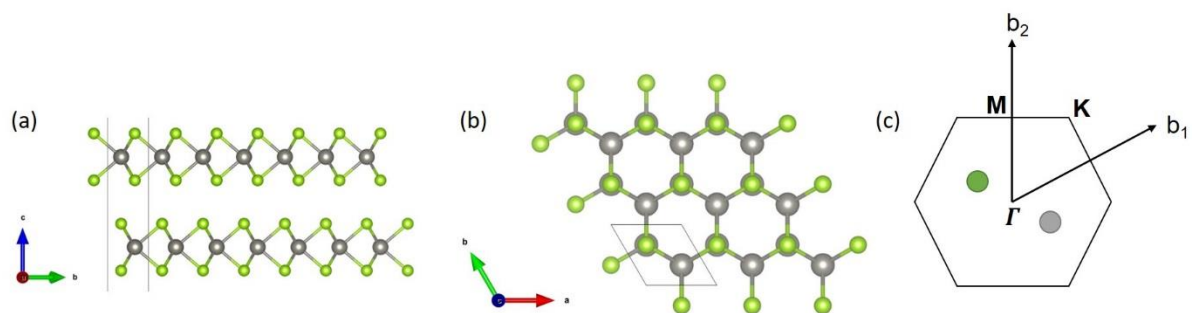


Figure S2. The optimized structure of BL WSe₂ in (a) side-view and (b) top-view. The grey and green balls represent W atoms and Se atoms, respectively. The solid lines demonstrate the primitive cell. The vectors of the real space were illustrated in the left sides. (c) The reciprocal cell of the BL WSe₂.

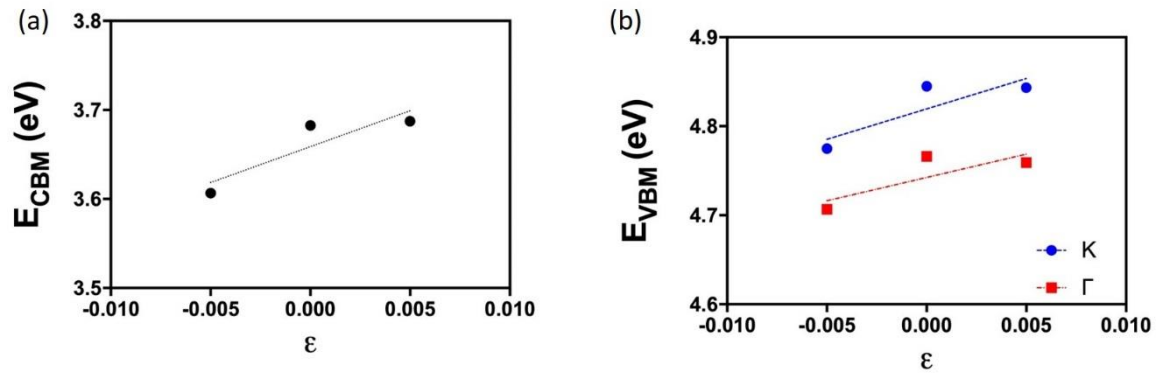


Figure S3. The absolute values of conduction band minimum and valence band maximum (both Γ and K) of BL WSe₂ under longitudinal strain along b (denoted in Figure S2a and b).

Due to the nature of the competing valence band maximum (VBM) at Γ and K points (Figure S1b), both effective mass of holes at these points were calculated along different directions. Here we denoted the $m_{h,\Gamma \rightarrow M}^*$, $m_{h,\Gamma \rightarrow K}^*$, $m_{h,K \rightarrow \Gamma}^*$ and $m_{h,K \rightarrow M}^*$. Similarly, the effective mass of the electron at the conduction band minimum (CBM) at K along two directions were denoted as were $m_{e,K \rightarrow \Gamma}^*$ and $m_{e,K \rightarrow M}^*$. For the reciprocal vectors in three directions were

$$\partial k_{K \rightarrow M} = 0.0471525 \text{ \AA}^{-1}$$

$$\partial k_{K \rightarrow \Gamma} = 0.0544447 \text{ \AA}^{-1}$$

$$\partial k_{\Gamma \rightarrow K} = 0.108894 \text{ \AA}^{-1}$$

According to the Equation (1), the effective masses were listed in Table S1

Table S1. The calculated effective mass of the electron (in m_0) at conduction band minimum and valence band maximum at different reciprocal directions.

	$K \rightarrow \Gamma$	$K \rightarrow M$	$\Gamma \rightarrow K$	$\Gamma \rightarrow M$
m_e^*	2.51	3.27	N/A	N/A
m_h^*	2.41	2.20	4.44	1.11

As shown in the Figure 2f – h, where chalcogen play the essential role in the WSe₂, it suggests the primary charge carrier transportation direction is along the a direction in the real space (Figure S2a and b). This direction corresponds to $\Gamma \leftrightarrow K$ (Figure S2c). Hence, the elastic modulus could be calculated according to

$$C_{2D} = A_0^{-1} \frac{\partial^2 E}{\partial \epsilon^2} \quad (\text{S1})$$

Where the A_0 is the area of the cross-section. Hence, the calculated $C_{2D} = 7.38 \times 10^{-4} \text{ eV \AA}^{-2}$. Further, the effective mass of electron and hole was taken as the average between $K \rightarrow \Gamma$ and $K \rightarrow M$, where

$$m_{h,K}^* = (m_{h,K \rightarrow \Gamma}^* \times m_{h,K \rightarrow M}^*)^{\frac{1}{2}} \quad (\text{S2})$$

$$m_{h,\Gamma}^* = (m_{h,\Gamma \rightarrow M}^* \times m_{h,\Gamma \rightarrow K}^*)^{\frac{1}{2}} \quad (S3)$$

$$m_e^* = (m_{e,K \rightarrow \Gamma}^* \times m_{e,K \rightarrow M}^*)^{\frac{1}{2}} \quad (S4)$$

The deformation constant was determined by the absolute value of the CBM and VBM according to the strain (Figure S3). The absolute value of the Fermi level was calculated by the following:

$$W = \varphi_{vac} - E_f$$

The vacuum level was set to zero.

From linear fitting (Figure S5), the deformation constant (in eV) is

$E_d^{CBM,K}$	8.065
$E_d^{VBM,G}$	5.241
$E_d^{VBM,K}$	6.839

According to Equation (2), the scattering time (τ in ns) could be resulted in

Table S2. The electron and hole scattering time (ns) at K and Γ .

τ_K^e	0.796
τ_G^h	2.431
τ_K^h	1.377

Hence, even valence band of BL is higher in Γ than K, the scattering time at K outperforms is in Γ .

Finally, the electron and hole mobility (in $10^4 \text{ cm}^2 \text{ V}^{-1} \text{ s}^{-1}$) at Γ and K are:

Table S3. The electron and hole mobility (in $10^4 \text{ cm}^2 \text{ V}^{-1} \text{ s}^{-1}$) at K and Γ point.

	K	Γ
Electron	49.01	
hole	105.50	193.26